# SelfDRSC++: Self-Supervised Learning for Dual Reversed Rolling Shutter Correction

Wei Shang, Dongwei Ren, Wanying Zhang, Qilong Wang, Pengfei Zhu, and Wangmeng Zuo

Abstract—Modern consumer cameras commonly employ the rolling shutter (RS) imaging mechanism, via which images are captured by scanning scenes row-by-row, resulting in RS distortion for dynamic scenes. To correct RS distortion, existing methods adopt a fully supervised learning manner that requires high framerate global shutter (GS) images as ground-truth for supervision. In this paper, we propose an enhanced Self-supervised learning framework for Dual reversed RS distortion Correction (SelfDRSC++). Firstly, we introduce a lightweight DRSC network that incorporates a bidirectional correlation matching block to refine the joint optimization of optical flows and corrected RS features, thereby improving correction performance while reducing network parameters. Subsequently, to effectively train the DRSC network, we propose a self-supervised learning strategy that ensures cycle consistency between input and reconstructed dual reversed RS images. The RS reconstruction in SelfDRSC++ can be interestingly formulated as a specialized instance of video frame interpolation, where each row in reconstructed RS images is interpolated from predicted GS images by utilizing RS distortion time maps. By achieving superior performance while simplifying the training process, SelfDRSC++ enables feasible one-stage self-supervised training. Additionally, besides start and end RS scanning time, SelfDRSC++ allows supervision of GS images at arbitrary intermediate scanning times, thus enabling the learned DRSC network to generate high framerate GS videos. On synthetic dataset, SelfDRSC++ achieves better or comparable quantitative metrics in comparison to state-of-the-art methods trained with the full supervision manner. Our SelfDRSC++ can produce high framerate GS videos with finer correction textures and better temporary consistency when dealing with real-world RS cases. The code and trained models are available at https://github.com/shangwei5/SelfDRSC\_plusplus.

Index Terms—Self-supervised learning, rolling shutter correction, dual reversed imaging mechanism.

# 1 Introduction

R ECENT years have witnessed an increasing demand for imaging sensors, due to the widespread applications of digital ECENT years have witnessed an increasing demand for imagcameras and smartphones. Although the Charge-Coupled Device (CCD) has been the dominant technology for imaging sensors, it is recently popular that modern consumer cameras choose the Complementary Metal-Oxide Semiconductor (CMOS) as an alternative due to its many merits, e.g., easy integration with image processing pipeline and communication circuits, and low power consumption [22]. In CMOS sensors, rolling shutter (RS) scanning mechanism is generally deployed to capture images, i.e., each row of CMOS array is exposed in the sequential time, which is different from CCD with global shutter (GS) scanning at one instant. Therefore, RS images suffer from distortion when capturing dynamic scenes, which not only affect human visual perception but also yield performance degradation or even failure in computer vision tasks [2], [19].

To correct RS distortion, pioneering works usually reconstruct GS images from a single RS image [27], [43] or multiple consecutive RS images [8], [9], [11], [23], where the latter ones usually

Wei Shang is with the Faculty of Computing, Harbin Institute of Technology, Harbin, China. (E-mail: csweishang@gmail.com)

Dongwei Ren is with the Faculty of Computing, Harbin Institute of Technology, Harbin, China. (Corresponding Author. E-mail: rendongweihit@gmail.com) Wanying Zhang is with the Faculty of Computing, Harbin Institute of Technology, Harbin, China. (E-mail: swzwanying@gmail.com)

Qilong Wang is with the Tianjin Key Laboratory of Machine Learning, College of Intelligence and Computing, Tianjin University, Tianjin, China. (E-mail: qlwang@tju.edu.cn)

Pengfei Zhu is with the Tianjin Key Laboratory of Machine Learning, College of Intelligence and Computing, Tianjin University, Tianjin, China. (E-mail: zhupengfei@tju.edu.cn)

Wangmeng Zuo is with the Faculty of Computing, Harbin Institute of Technology, Harbin, China. (E-mail: wmzuo@hit.edu.cn)

have better performance. But the consecutive RS image setting is ambiguous [40], e.g., two RS cameras, moving horizontally at the same speed but with different readout time, can produce the same RS images. To address this ambiguity, a new RS acquisition setting, i.e., dual RS images with reversed scanning directions (see Fig. 1), is proposed in [1], [40]. In [1], one GS image is reconstructed from dual RS images with reversed distortion, while in [40], Zhong et al. devote efforts to reconstruct high framerate GS videos. Nevertheless, both of them adopt a fully supervised learning manner, i.e., ground-truth GS images are required for supervised learning RS correction networks. Especially in [40], high framerate GS videos should be collected to serve as groundtruth. However, it is not easy to collect real-world training samples, while synthetic training samples yield poor generalization ability when handling real-world RS cases. Recently, Qu et al. [29], [30] proposed a geometry-based pixel-wise correction solver to correct RS image by rescaling its corresponding optical flow vector. Although this method does not require supervised training, it needs knowledge of the RS exposure time and readout, making it impractical for real-world RS cases where manual adjustment of these hyper-parameters is not feasible. Additionally, the method utilizes backward warping for RS correction, which leads to boundary loss such as black edges in the resulting images.

In this paper, we aim ambitiously for the more challenging and practical task, *i.e.*, self-supervised learning to invert dual reversed RS images to a high framerate GS video. As shown in Fig. 2, our proposed SelfDRSC++ consists of two key modules, *i.e.*, a dual reverse RS correction (DRSC) network  $\mathcal{F}$  for correcting RS distortion and an RS reconstruction module  $\mathcal{W}$  to enable feasible self-supervised learning. For the DRSC network design in Fig. 3, we draw inspiration from optical flow estimation [34] and video frame



Fig. 1. Illustration of capturing dual RS images with reversed scanning directions, *i.e.*, top-to-bottom ( $I_{t2b}$ ) and bottom-to-top ( $I_{b2t}$ ). In this work, we propose a more effective self-supervised learning method SelfDRSC++ to correct RS distortion. In comparison to state-of-the-art supervised RS correction methods CVR [10] and IFED [40], our SelfDRSC++ can generate high framerate GS videos with finer textures and better temporary consistency.

interpolation (VFI) method [21]. Specifically, we adopt a joint optimization for optical flows and corrected features to compact the structure and refine them further by leveraging the correlation volume matching block in [34]. Our self-supervised learning strategy is guided by the principle that the DRSC network's predicted latent GS images can be utilized to reconstruct dual RS images with reversed distortion, thereby enabling the training of the DRSC network by enforcing cycle consistency between input and reconstructed RS images. To achieve this, we propose a VFIbased RS reconstruction module (as depicted in Fig. 4), which considers RS reconstruction as a specialized case of video frame interpolation by using a distorted time map to substitute distance indexing in VFI method [41]. Finally, we employ a self-supervised loss function to train the DRSC network. During the training process, an intermediate GS image at arbitrary RS scanning time is predicted, corresponding to which another set of dual RS images can be reconstructed in our VFI-based RS reconstruction module. Consequently, the predicted GS images at intermediate scanning time in SelfDRSC++ can also be supervised, making the learned DRSC network be able to generate high framerate GS videos.

Extensive experiments on synthetic and real-world RS images have been conducted to evaluate our SelfDRSC++. Although any ground-truth GS images are not used in the training phase of our SelfDRSC++, it still achieves comparable quantitative metrics on synthetic datasets, in comparison to state-of-the-art supervised RS correction methods. In real-world RS cases, our SelfDRSC++ can produce high framerate GS videos with finer textures and better temporary consistency.

This work is previously presented as a conference paper [32], where the DRSC network is borrowed from IFED [40] and the self-supervised training is conducted in two stages to address boundary artifacts in corrected results. In this manuscript, our major improvements include (i) a more compact and lightweight DRSC network that can improve correction performance with reduced network parameters, (ii) a one-stage self-supervised training strategy that is able to effectively train DRSC network, and (iii) inclusion of more state-of-the-art methods such as JAM [11], LBCNet [9] and V-DRSC [30] for experimental comparison. To sum up, the contributions of this work are three-fold:

 We propose SelfDRSC++, a self-supervised learning framework, for achieving real-world RS correction from dual reversed RS images without the need for high framerate GS videos as ground-truth.

- The RS reconstruction module in SelfDRSC++ is intriguingly formulated as a specialized instance of VFI, enabling one-stage self-supervised learning for DRSC networks while effectively mitigating boundary artifacts.
- We present a compact and lightweight RS correction network, which significantly surpasses state-of-the-art methods in terms of correction textures for dealing with real-world RS cases.

The remainder of this paper is structured as follows: Section 2 provides a comprehensive review of the relevant literature, Section 3 introduces our proposed DRSC network and self-supervised training strategy, Section 4 experimentally validates the effectiveness of the proposed approach, and finally Section 5 concludes this paper by summarizing key findings.

# 2 RELATED WORK

## 2.1 Rolling Shutter Distortion Correction

With the rising demand for RS cameras, RS distortion corrections have received widespread attention. Existing works on RS correction generally fall into two categories: single-image-based [27], [43] and multi-frame-based [8], [9], [11], [23], [30], [32], [40] methods. It is an ill-posed problem to correct RS distortion from a single image, and its performance is usually inferior. For multiframe-based methods, can be further divided into generating one specific image and generating a video sequence. For the former, Liu et al. [23] proposed an end-to-end model, which warped features of RS images to a GS image by a special forward warping block. For the latter, Fan et al. [8] designed a deep learning framework, which utilized the underlying spatio-temperal geometric relationships for generating a latent GS image sequence. Then Fan et al. [10] further proposed a context-aware model for solving complex occlusions and object-specific motion artifacts. Recently, Zhong et al. [40] proposed an end-to-end method IFED, and it can extract an undistorted GS sequence grounded on the symmetric and complementary nature of dual RS images with reversed distortion [1]. Fan et al. [11] refined GS appearance features together with bidirectional motion fields in a singlestage framework for more efficient RS correction. However, these methods all rely on supervised learning, which would yield poor generalization on real-world data. To solve this problem, Ou et al. [30] proposed an efficient geometry-based method, which can correct RS frames according to the optical flows of RS

frames. And Shang *et al.* [32] designed a bidirectional distortion warping module to reconstruct dual reversed RS images, forming self-supervision between input and reconstructed dual reversed RS images. Wang *et al.* [35] integrated event data, leveraging cycle consistency, latent consistency, and temporal consistency to accomplish self-supervised learning for RS correction.

# 2.2 Cycle Consistency-based Self-supervised Learning in Low-level Vision

The concept of cycle consistency has been utilized in several lowlevel vision tasks for self-supervised learning. Zhu et al. [42] proposed a cycle consistency loss for unpaired image-to-image translation. Chen et al. [5] enforced the results by fine-tuning existing methods in a self-supervised fashion, where they estimated the per-pixel blur kernel based on optical flows between restored frames, for reconstructing blurry inputs. Ren et al. [31] utilized two generative networks for respectively modeling the deep priors of clean image and blur kernel to reconstruct blurred image for enforcing cycle consistency. Liu et al. [24] claimed that motion cues obtained from consecutive images yield sufficient information for deblurring task and they re-rendered the blurred images with predicting optical flows for cycle consistency-based self-supervised learning. Bai et al. [3] presented a self-supervised video superresolution method, which can generate auxiliary paired data from the original low resolution input videos to constrain the network training. Shang et al. [32] proposed a self-supervised learning method SelfDRSC, which uses a bidirectional distortion warping module to reconstruct dual reversed RS images. Moreover, a selfdistillation strategy is proposed to mitigate boundary artifacts in generated GS images. To sum up, in these methods, degraded images can be reconstructed based on the imaging mechanism, and then self-supervised loss can be employed to enforce the cycle consistency between reconstructed and original degraded images. In this work, we further refine two main components of SelfDRSC. We integrate a joint optimization approach from VFI methods for both optical flows and features to further reduce the parameters of the correction network. Concurrently, we introduce a novel RS image reconstruction method that replaces the bidirectional distortion warping module in SelfDRSC, enhancing the correction effect and avoiding boundary artifacts.

#### 2.3 Video Frame Interpolation

With the resurgence of deep learning, frame rate upconversion [6], [7], [13] has reemerged in the field of computer vision under the name of video frame interpolation. Both Center-Frame Interpolation [4], [20], [28] and Multi-Frame Interpolation [12], [14], [21], [37], [38] have been extensively investigated. For center-frame interpolation, Niklaus et al. [28] proposed separable kernel prediction networks to handle large motion and optimized it through a 'perceptual' loss [15]. Bao et al. [4] suggested the incorporation of depth information during the interpolation process, combating occlusions through bidirectional flow estimation. Lee et al. [20] combined and generalized kernel-based and flow-based methods by offset prediction and introduced an adversarial loss to inspect the naturalness of the interpolated frame relative to adjacent input frames. For multi-frame interpolation, more complex motion trajectory models need to be specified compared to the linear model assumption typically used in center-frame interpolation. Xu et al. [37] proposed a quadratic interpolation scheme to allow the inter-motion to be curvilinear. Huang et al. [12] and

Kong et al. [17] designed an efficient pyramid network and utilized the so-called privileged distillation scheme for real-time arbitrary timestamp frame interpolation. In addition, Kalluri et al. [16] utilized 3D convolutions to extract spatiotemporal features for multi-frame interpolation. Shang et al. [33] considered the motion-induced blur in video sequences and achieved joint video frame interpolation and deblurring. Recently, advanced network modules and operations have been proposed to further enhance the performance of VFI. For instance, the unified operation in EMA-VFI [38] explicitly separates motion and appearance information, and the AMT [21] employs bidirectional correlation volumes for all pixel pairs, which are inspired by RAFT [34]. Zhong et al. [41] introduced distance indexing and an iterative referencebased estimation strategy in a plug-and-play manner to enhance the performance of video interpolation. All these methods would encounter difficulties when the camera employs a GS mechanism because they can not correctly synthesize the in-between frames in the case of RS images.

# 3 Proposed Method

In this section, we initially present the problem formulation of self-supervised learning for Dual reversed RS Correction. Subsequently, we provide a comprehensive introduction to the architecture of the correction network and elaborate on the specifics of the self-supervised learning strategy.

#### 3.1 Formulation of SelfDRSC++

Recently, dual reversed RS imaging setting [1], [32], [40] has been proposed to address the ambiguity issue in consecutive RS images, where two RS images are captured simultaneously by different scanning patterns, i.e., top-to-bottom ( $I_{t2b} \in \mathbb{R}^{H \times W \times 3}$ ) and bottom-to-top ( $I_{b2t} \in \mathbb{R}^{H \times W \times 3}$ ), as shown in Fig. 1. We first give a formal imaging formation of dual RS images with H rows. Without loss of generality, we define the acquisition time t as the midpoint of the whole exposure period, i.e., each RS image is captured from  $t_1$  to  $t_H$ , having H-1 readout instants  $\tau$ , where start scanning time  $t_1 = t - \tau (H-1)/2$  and end scanning time  $t_H = t + \tau (H-1)/2$ . Dual reversed RS images captured at time t can be defined as

$$\begin{split} & \boldsymbol{I}_{t2b}^{(t)}[i] = \boldsymbol{I}_g^{(t+\tau(i-(H+1)/2))}[i], \\ & \boldsymbol{I}_{b2t}^{(t)}[i] = \boldsymbol{I}_g^{(t+\tau(i-(H+1)/2))}[H-i+1], \end{split} \tag{1}$$

where  $I_g$  is the latent GS image. When scanning i-th rows for  $I_{t2b}^{(t)}$  and  $I_{b2t}^{(t)}$ , the image contents are captured from  $I_g$  at the same instant time  $t_i$  but with reversed scanning directions. In the following, the superscripts in  $I_{t2b}^{(t)}$  and  $I_{b2t}^{(t)}$  are omitted, since  $t=(t_1+t_H)/2$ .

Under the dual reversed RS imaging setting, RS distortion can be well distinguished, *i.e.*, dual reversed RS images  $\boldsymbol{I}_{t2b}$  and  $\boldsymbol{I}_{b2t}$  provide cues for reconstructing GS images between  $t_1$  and  $t_H$ , even for the ambiguous case in the consecutive video setting. In the most recent state-of-the-art method IFED [40], fully supervised learning is employed for learning DRSC network, where high framerate GS video frames should be collected as ground-truth supervision. Albeit obtaining promising performance, high framerate GS frames are not trivial to collect. The common solution is to synthesize training datasets where video frame interpolation is usually adopted to increase video framerate [40], thus restricting their performance in real-world cases.

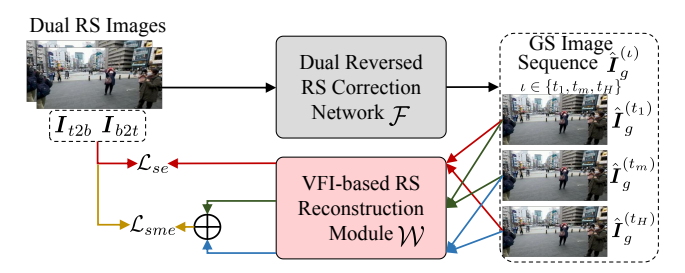


Fig. 2. Training framework of our SelfDRSC++, which consists of two key modules, i.e., DRSC network  $\mathcal F$  for generating GS images  $\{\hat I_g^{(t_1)},\hat I_g^{(t_m)},\hat I_g^{(t_H)}\}$  from input dual RS images  $I_{t2b}$  and  $I_{b2t}$ , and a VFI-based RS reconstruction module  $\mathcal W$  for reconstructing dual reversed RS images. Finally, self-supervised loss  $\mathcal L_{se}$  and  $\mathcal L_{sme}$  for enforcing the cycle consistency between input and reconstructed RS images can be employed. Details regarding  $\mathcal F$  and  $\mathcal W$  can be found in Figs. 3 and 4, respectively.

In this work, we propose a novel self-supervised learning method, SelfDRSC++, for rolling shutter correction with dual reversed distortion, where only RS images are required for training DRSC network, without the need for ground-truth high framerate GS images. Formally, the optimization of our method is defined as

$$\min_{\boldsymbol{\Theta}} \mathcal{L}\left(\left\{\boldsymbol{I}_{t2b}, \boldsymbol{I}_{b2t}\right\}, \mathcal{W}\left(\mathcal{F}\left(\boldsymbol{I}_{t2b}, \boldsymbol{I}_{b2t}; \boldsymbol{\Theta}\right)\right)\right), \tag{2}$$

which contains two key components: dual reversed RS correction network  $\mathcal F$  with parameters  $\Theta$ , a VFI-based RS reconstruction module  $\mathcal W$ . And then self-supervised learning objective  $\mathcal L$  can be adopted to enhance the consistency between input and reconstructed RS images. Our self-supervised framework is depicted in Fig. 2. Different from SelfDRSC [32], we draw upon methods from video frame interpolation [21] and video RS correction [11], employing a joint optimization of optical flows and corrected features to further reduce parameters of module  $\mathcal F$ . Additionally, we adopt the correlation matching block [34] to assist in refining the estimated optical flows. For the RS reconstruction module  $\mathcal W$ , we employ a VFI method based on distorted time maps, which demonstrates superior RS reconstruction performance. This, in turn, enhances the effectiveness of self-supervised training, as analyzed in Sec. 4.4.

## 3.2 Network Architecture of DRSC $\mathcal{F}$

The architecture of  $\mathcal{F}$  consists of a multi-scale bidirectional RS correction module and a multi-field GS reconstruction module, as shown in Fig. 3. During training phase, our distortion correction network  $\mathcal{F}$  generates three images  $\{\hat{I}_g^{(t_1)}, \hat{I}_g^{(t_m)}, \hat{I}_g^{(t_H)}\}$  where  $t_m$  is an intermediate scanning time between start time  $t_1$  and end time  $t_H$ . During the inference phase, it allows the distortion correction network to generate videos with arbitrary framerate by giving different intermediate scanning times. In the following, we take an example to show how intermediate GS image  $\hat{I}_g^{(t_m)}$  is predicted from dual reversed RS images  $I_{b2t}$  and  $I_{t2b}$ . The start and end GS images  $\hat{I}_g^{(t_1)}$  and  $\hat{I}_g^{(t_H)}$  can be obtained in the same way.

# 3.2.1 RS Correction Module

For inverting RS images to GS images, a natural strategy is to warp RS images based on the optical flow  $F_{g \to t2b}^{(t_m)}$  and  $F_{g \to b2t}^{(t_m)}$  between input RS images and latent GS images. However, these methods do not facilitate the interaction of complementary motion and context

features. Recently, Fan *et al.* [11] proposed JAM to simultaneously refine the global shutter features and undistortion motion field. Following [11], [21], we adopt a multi-scale bidirectional RS correction module to update bidirectional flows and extract intermediate features jointly. Specifically, our module comprises two encoders and a decoder. The two encoders are designed to encode distinct features, where one encoder is tasked with extracting correlation features to compute bidirectional correlation volumes, while the other is dedicated to capturing content features for predicting corrected features. We in the following introduce the two encoders and the decoder in detail.

The correlation encoder comprises 4 scales, with each scale consisting of three blocks. Each block within the encoder contains a convolutional layer, followed by an instance normalization layer, and concludes with a ReLU activation function. We compute the dot-product similarities between the output features  $G_{t2b}$ ,  $G_{b2t} \in \mathbb{R}^{\frac{H}{8} \times \frac{W}{8} \times C}$  for constructing a 4D correlation volume, and this process can be written as

$$V[i, j, k, l] = \sum_{h} G_{t2b}[i, j, h] \cdot G_{b2t}[k, l, h],$$
 (3)

where  $V \in \mathbb{R}^{rac{H}{8} imes rac{W}{8} imes rac{H}{8} imes rac{W}{8}}.$  In order to compute the correlation volume at different scales, we perform average pooling on the last two dimensions of V to achieve downsampling, with a kernel size of 2 and a stride of 2. We thus obtain multiscale correlation volumes  $\{V_1, V_2, V_3, V_4\}$ . To obtain the bidirectional correlation volume, and to avoid redundant computations, we transpose the matrix V to obtain  $V^T$ , which serves as the reverse correlation volume. Also, we can get the multiscale reverse correlation volumes  $\{V_1^T, V_2^T, V_3^T, V_4^T\}$ . Correspondingly, our context encoder also generates features at four scales for each RS, denoted as  $\{X_{t2b,1}, X_{t2b,2}, X_{t2b,3}, X_{t2b,4}\}$ and  $\{X_{b2t,1}, X_{b2t,2}, X_{b2t,3}, X_{b2t,4}\}$ . This enables matching and searching with the correlation volumes in each scale of the subsequent decoder, thereby jointly updating the estimated optical flows and the corrected features. The design of the context encoder is quite similar to that of the correlation encoder, with the exception that the instance normalization layer has been removed, and the ReLU activation function has been replaced with PReLU.

The decoder also contains 4 scales. Except for the last scale, each scale contains a joint upsampling block, a correlation volume matching block, and an updating block. Given that the decoder aims to jointly optimize the optical flows and the corrected features, it is imperative to provide temporal information. Unlike video frame interpolation tasks, which only require the time instance to interpolate the frame, due to the imaging mechanism of RS, we can obtain the time displacement between the input RS image and the target GS image. Formally, the values at *i*-th row in time displacement are given by

$$\mathbf{D}_{g \to t2b}^{(t_m)}[i] = \frac{i - m}{H - 1}, & i, m \in [1, \dots, H], \\
\mathbf{D}_{g \to b2t}^{(t_m)}[i] = \frac{(H - i) - (m - 1)}{H - 1}, & i, m \in [1, \dots, H].$$
(4)

This temporal displacement is crucial for the decoder to effectively integrate temporal cues into the optimization process. Then we elaborate on each block in detail, taking the d-th scale  $(d \in \{4,3,2\})$  as an example.

$$\begin{aligned} & F_{g \to t2b,d-1}^{(t_m)}, F_{g \to b2t,d-1}^{(t_m)}, & X_{g,d-1}^{(t_m)} = \\ & \text{UConv}(F_{g \to t2b,d}^{(t_m)}, F_{g \to b2t,d}^{(t_m)}, & X_{g,d}^{(t_m)}, & X_{t2b,d}, & X_{b2t,d}), \end{aligned} \tag{5}$$

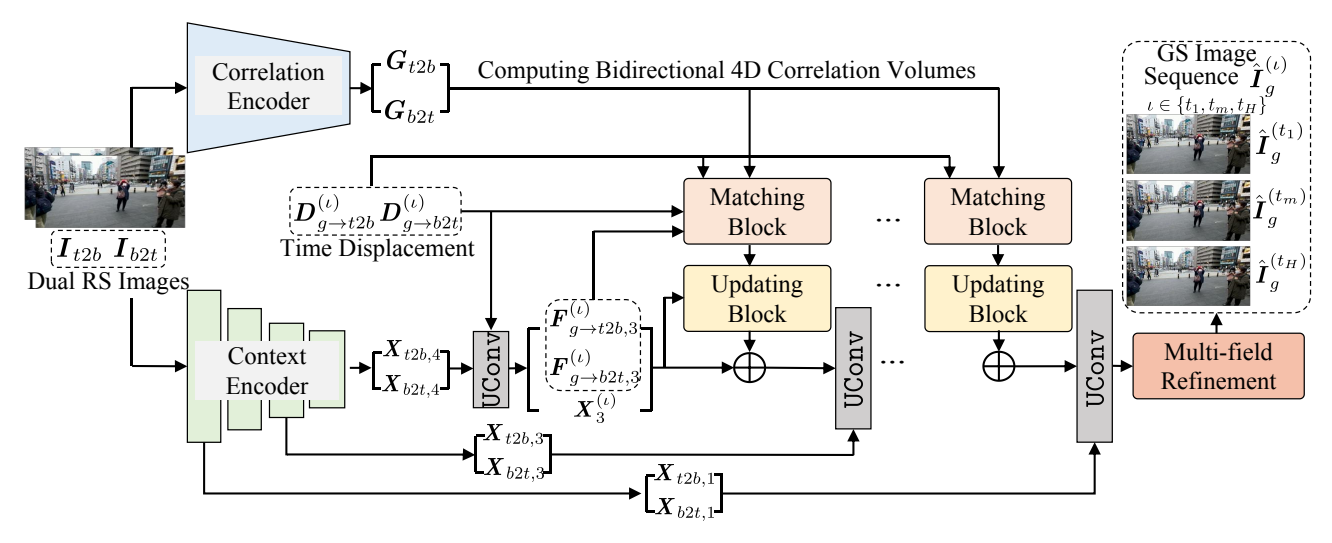


Fig. 3. Architecture of the DRSC network  $\mathcal{F}$ . The network can correct dual RS images to GS images according to time displacements. It primarily consists of two encoders that extract correlation features  $\{G_{t2b}, G_{b2t}\}$ , and content features  $\{X_{t2b,d}, X_{b2t,d}\}(d \in \{4,3,2,1\})$ , followed by a decoder with each scale comprising a joint upsampling block (UConv), a matching block, and an updating block. The final output from the last decoder layer is integrated through a multi-field refinement Eq. (9) to form the final GS image.

where  $UConv(\cdot)$  denotes the joint upsampling block. Specifically, within the  $UConv(\cdot)$ , the inputs – optical flows, RS features, and corrected RS features – are initially processed through a single ResBlock and a transposed convolution layer to obtain relative motion maps between the latent GS images and the input RS images.

$$\begin{split} & O_{g \to t2b, d-1}^{(t_m)}, O_{g \to b2t, d-1}^{(t_m)}, & X_{g, d-1}^{(t_m)} = \\ & \texttt{DConv}(F_{g \to t2b, d}^{(t_m)}, F_{g \to b2t, d}^{(t_m)}, & X_{g, d}^{(t_m)}, & X_{t2b, d}, & X_{b2t, d}), \end{split} \tag{6}$$

where  $\mathrm{DConv}(\cdot)$  denotes one ResBlock and one transposed convolution layer.  $O_{g \to t2b,d-1}^{(t_m)}$  and  $O_{g \to b2t,d-1}^{(t_m)}$  are estimated relative motion maps between latent GS images and the input RS images. Then the optical flows between input RS images and latent GS images can be obtained by multiplying corresponding time displacement and relative motion map in an entry-by-entry manner, i.e.,  $\widetilde{F}_{g \to t2b,d-1}^{(t_m)} = D_{g \to t2b,d-1}^{(t_m)} \odot O_{g \to t2b,d-1}^{(t_m)}$  and  $\widetilde{F}_{g \to b2t,d-1}^{(t_m)} = D_{g \to b2t,d-1}^{(t_m)} \odot O_{g \to b2t,d-1}^{(t_m)}$ . We employ bilinear interpolation on time displacement at various scales to ensure that its spatial size is aligned with those of relative motion maps. The corrected features can be obtained from  $X_{t2b,d-1}$  and  $X_{b2t,d-1}$  by the backward warping operation with the optical flows. The corrected features are concatenated with other features along the channel dimension dubbed  $\widetilde{X}_{g,d-1}^{(t_m)}$ , combined with the optical flows, and finally fed into a ResBlock Sconv,

$$\begin{split} \hat{\pmb{F}}_{g \to t2b, d-1}^{(t_m)}, \hat{\pmb{F}}_{g \to b2t, d-1}^{(t_m)}, \hat{\pmb{X}}_{g, d-1}^{(t_m)} = \\ \text{SConv}(\widetilde{\pmb{X}}_{g, d-1}^{(t_m)}, \widetilde{\pmb{F}}_{g \to t2b, d}^{(t_m)}, \widetilde{\pmb{F}}_{g \to b2t, d}^{(t_m)}). \end{split} \tag{7}$$

When d=4, due to the absence of relative motion maps, we cannot obtain the optical flow. Consequently, the optical flows  $F_{g \to t2b,d}^{(t_m)}$  and  $F_{g \to b2t,d}^{(t_m)}$  are omitted from the input in Eq. (5).

Subsequently, we use a correlation volume matching block to search the bidirectional correlation volumes through predicted optical flows, akin to the procedure in RAFT [34]. We construct two search windows centered around the bidirectional flow with the predefined window size. The search operation within these windows is conducted across all scales of the bidirectional correlation volume. The matched bidirectional correlations are

concatenated into a feature map to further jointly update the optical flows and the corrected features.

Finally, we employ an update block to jointly predict the residuals of the optical flows and the corrected features based on the matched bidirectional correlations. In each update block, the bidirectional correlation features and the bidirectional optical flows are first passed through two convolutional layers and LeakyReLU activations in between. Then, they are concatenated with the corrected features and then fed into two additional convolutional layers and LeakyReLU activations in between. Finally, the output features are sent to two separate heads for predicting bilateral flow residuals  $\Delta F_{g \to t2b,d-1}^{(t_m)}$ ,  $\Delta F_{g \to b2t,d-1}^{(t_m)}$ , and the corrected features residual  $\Delta X_{g,d-1}^{(t_m)}$ . Each head is formed by two convolutional layers and LeakyReLU activations in between. The predicted optical flows residual and the corrected features residual are added back to the output of Eq. (7) to complete the update of the optical flows and the corrected features by

$$\begin{split} & \pmb{F}_{g \to t2b, d-1}^{(t_m)} = \Delta \pmb{F}_{g \to t2b, d-1}^{(t_m)} + \hat{\pmb{F}}_{g \to t2b, d-1}^{(t_m)}, \\ & \pmb{F}_{g \to b2t, d-1}^{(t_m)} = \Delta \pmb{F}_{g \to b2t, d-1}^{(t_m)} + \hat{\pmb{F}}_{g \to b2t, d-1}^{(t_m)}, \\ & \pmb{X}_{g \to g, d-1}^{(t_m)} = \Delta \pmb{X}_{g, d-1}^{(t_m)} + \hat{\pmb{X}}_{g, d-1}^{(t_m)}. \end{split} \tag{8}$$

The updated outputs serve as the input for UConv in the subsequent scale.

The last scale (d=1) of the decoder only contains a joint upsampling block. Distinguished from Eq. (5), the current formulation yields outputs that encompass image residuals  $R^{(t_m)}$  and occlusion masks  $M^{(t_m)}$ , diverging from the output of corrected features. In addition, we adopt a reconstruction design inspired by AMT [21], which generates a group of optical flows, image residuals, and occlusion masks. These elements are curated to facilitate the forthcoming reconstruction of GS images.

# 3.2.2 GS Reconstruction Module

The remaining issue is how to fuse warped images for reconstructing latent GS image  $I_g^{(t_m)}$ . In flow-based VFI and RS correction

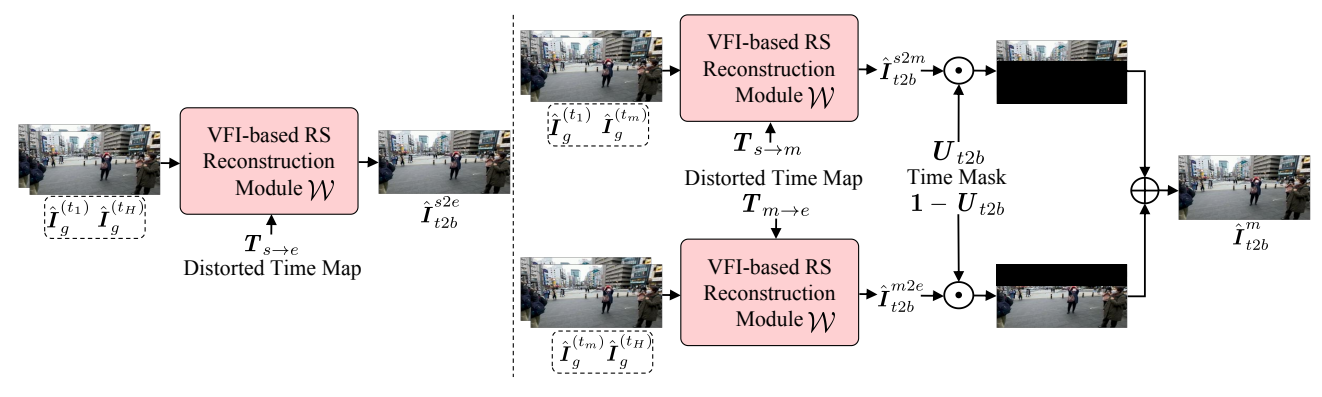


Fig. 4. VFI-based module  $\mathcal W$  for reconstructing dual reversed RS images.  $\mathcal W$  is capable of generating the corresponding RS image based on GS inputs and given distorted time maps. And module  $\mathcal W$  is frozen during the training process.

methods [21], [32], [40], the common solution for generating the final frame is

$$\hat{\boldsymbol{I}}_{g}^{(t_{m})} = \boldsymbol{R}^{(t_{m})} + \boldsymbol{M}^{(t_{m})} \odot \boldsymbol{W}_{t2b}^{(t_{m})} + (1 - \boldsymbol{M}^{(t_{m})}) \odot \boldsymbol{W}_{b2t}^{(t_{m})}, \quad (9)$$
 where  $\boldsymbol{W}_{t2b}^{(t_{m})} = \text{warp}(\boldsymbol{I}_{t2b}, \boldsymbol{F}_{g \to t2b}^{(t_{m})})$  and  $\boldsymbol{W}_{b2t}^{(t_{m})} = \text{warp}(\boldsymbol{I}_{b2t}, \boldsymbol{F}_{g \to b2t}^{(t_{m})})$  are obtained by the input RS images through a backward warping operation. However, predicting a single pair of flow fields overlooks the fact that each location within occluded regions has numerous potential pixels, thereby constraining the solution space of the results [21]. At this juncture, the previously output set of occlusion masks and image residuals comes into play, enabling the generation of multiple reconstruction GS images according to Eq. (9). Subsequently, the obtained results are concatenated along the channel dimension and then adaptively merged and refined through two convolutional layers and LeakyReLU

# 3.3 Self-supervised Learning for DRSC

activations in between to finalize the output  $\hat{I}_{a}^{(t_{m})}$ .

To learn the parameters  $\Theta$  of DRSC network  $\mathcal{F}$ , we need to introduce supervision on  $\{\hat{I}_g^{(t_1)},\hat{I}_g^{(t_m)},\hat{I}_g^{(t_H)}\}$ . Instead of collecting ground-truth GS images, we suggest that supervision can be exploited from the input RS images themselves. Generally, we introduce a VFI-based module  $\mathcal{W}$  to reconstruct dual reversed RS images as shown in Fig. 4, and self-supervised loss  $\mathcal{L}$  can be adopted to learn the parameters  $\Theta$  without ground-truth GS images.

# 3.3.1 Reconstruction of Dual Reversed RS Images

Based on RS imaging mechanism, generated start and end GS images  $\hat{I}_g^{(t_1)}$  and  $\hat{I}_g^{(t_{H})}$  can be accordingly exploited to reconstruct dual reversed RS images  $\hat{I}_{t2b}$  and  $\hat{I}_{b2t}$ . Besides start and end GS images, we also provide a way to reconstruct RS images  $\hat{I}_{t2b}^m$  and  $\hat{I}_{b2t}^m$  from intermediate GS images  $\hat{I}_g^{(t_m)}$ . In the following, we take the top-to-bottom scanning pattern as an example to show the reconstruction of  $\hat{I}_{t2b}$ .

Reconstructing RS Images from Start & End GS Frames  $\hat{I}_g^{(t_1)}$  and  $\hat{I}_g^{(t_1)}$ . The purpose of  $\mathcal{W}$  is to reconstruct RS images  $\hat{I}_{t2b}$  and  $\hat{I}_{b2t}$  from  $\hat{I}_g^{(t_1)}$  and  $\hat{I}_g^{(t_H)}$ . Contrary to the approach in [32], we no longer employ optical flow estimation for distorted warping, because the results trained with this method tend to introduce boundary artifacts [32]. These artifacts necessitate the use of further self-distillation techniques to mitigate, thereby increasing the complexity and duration of the training process.

Consequently, we adopt a more straightforward method to directly obtain the reconstructed RS images. In [41], a video frame interpolation method based on distance indexing is introduced to address the issues arising from the uncertainty of velocity in existing video frame interpolation methods. Interestingly, we regard the generation of RS images as a special type of frame interpolation task, where each row corresponds to a different time instance. We design a distortion time map for representing the interpolation time in each row. Given the corrected results  $\hat{I}_g^{(t_1)}$  and  $\hat{I}_g^{(t_H)}$ , we are able to derive a distorted time map  $T_{s \to e}$  from the start time to the end time, according to the imaging mechanism of RS

$$T_{s \to e}[i] = \frac{(i-1) \cdot \tau}{(H-1) \cdot \tau} = \frac{i-1}{H-1}, i \in [1, \dots, H].$$
 (10)

And we can also get  $T_{e \to s} = 1 - T_{s \to e}$ . Due to the extremely short readout time  $\tau$  for each row during the actual capture process (e.g., in a 720P video at 30 FPS, the average readout time per row is approximately  $\frac{1s}{30 \times 720} \approx 46 \mu s$ ). The motion within this extremely short period can be assumed to be linear. We employ the distorted time map in place of the distance indexing used in [41] to facilitate the generation of RS images, represented as

$$\hat{I}_{t2b}^{s2e} = \mathcal{W}(\hat{I}_g^{(t_1)}, \hat{I}_g^{(t_H)}, T_{s \to e}), 
\hat{I}_{t2b}^{e2s} = \mathcal{W}(\hat{I}_g^{(t_H)}, \hat{I}_g^{(t_1)}, T_{e \to s}).$$
(11)

Referring to [41], W can be an existing VFI algorithm, where we directly utilize the pre-trained model provided by [41], without further finetuning on RS correction data. Following [32], we utilize the distorted time maps as weights to combine the two, yielding the final reconstructed RS image through a weighted summation. The RS image  $\hat{I}_{t2b}$  is reconstructed as

$$\hat{I}_{t2b} = T_{e \to s} \odot \hat{I}_{t2b}^{s2e} + T_{s \to e} \odot \hat{I}_{t2b}^{e2s}.$$
 (12)

We can acquire  $\hat{I}_{b2t}$  in the same manner by vertically flipping the distorted time maps and then applying Eqs. (11) and (12) to obtain  $\hat{I}_{b2t}$ .

**Reconstructing RS Images Using Intermediate GS Frame**  $\hat{I}_g^{(t_m)}$ . Aiming to make SelfDRSC++ be able to generate GS frames at the time of arbitrary scanline, we also need to constrain the generated intermediate GS image  $\hat{I}_g^{(t_m)}$  in a similar way. The only distinction is that the generation of RS images is divided into two parts, *i.e.*, one is from  $t_1$  to  $t_m$  and the other one is from  $t_m$ 

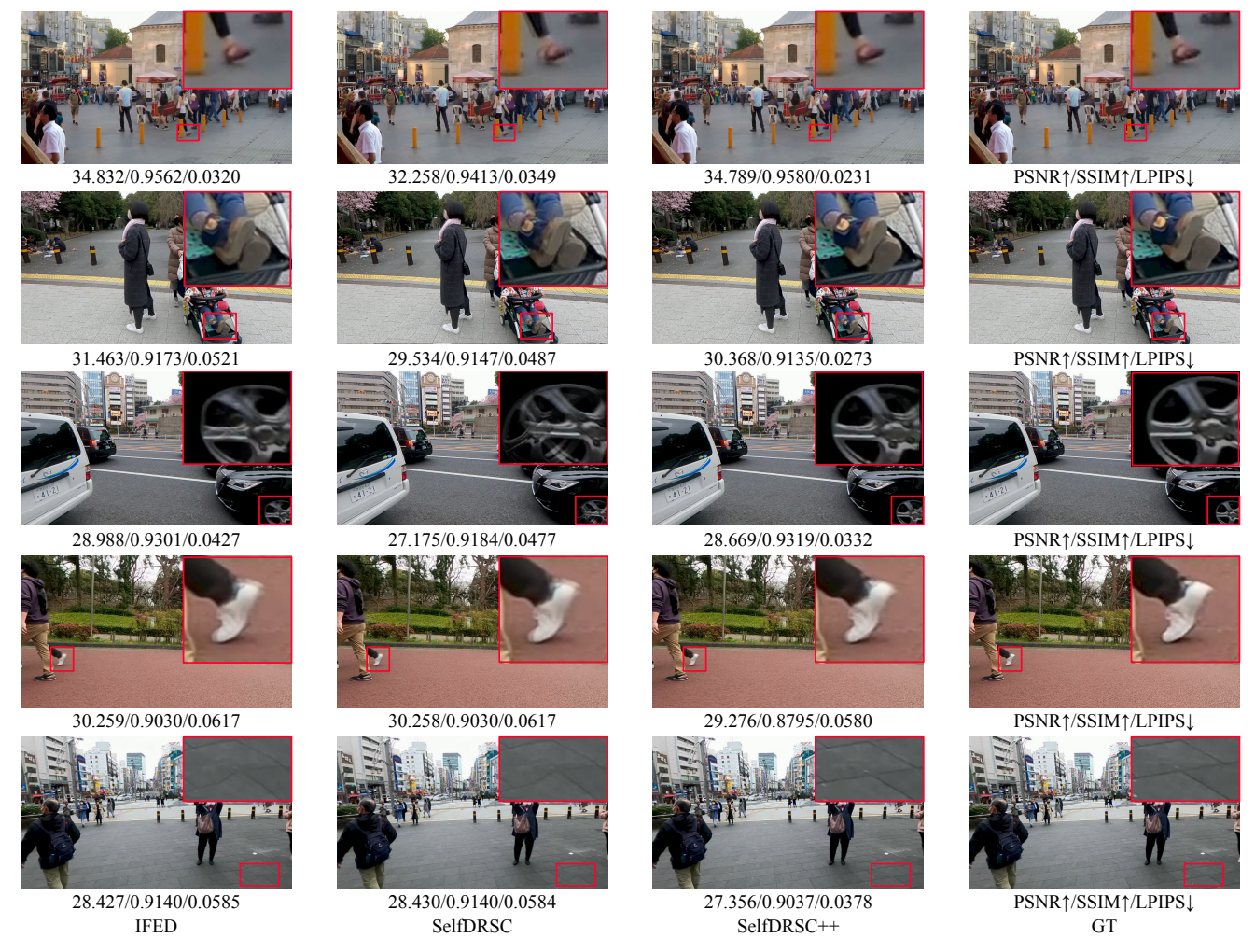


Fig. 5. Visual comparison on RS-GOPRO. Our SelfDRSC++ yields less ghosting while maintaining fine details. The evaluation metrics PSNR and SSIM tend to exhibit a preference for over-smoothed results, while LPIPS demonstrates a stronger correlation with human visual perception.

to  $t_H$ . According to Eq. (10), we can obtain distortion time map  $T_{s \to m}$  and  $T_{m \to e}$  as follows

$$\mathbf{T}_{s\to m}[i] = \begin{cases} \frac{i-1}{m-1}, & i \in [1, \dots, m], \\ 1, & i \in [m+1, \dots, H], \end{cases} 
\mathbf{T}_{m\to e}[i] = \begin{cases} 0, & i \in [1, \dots, m], \\ \frac{i-m-1}{H-m-1}, & i \in [m+1, \dots, H]. \end{cases}$$
(13)

Then we can obtain  $\hat{I}_{t2b}^{s2m}$  and  $\hat{I}_{t2b}^{m2e}$  similar to Eqs. (11) and (12). Finally, we can get the reconstructed RS frame  $\hat{I}_{t2b}^{m}$  with time mask  $U_{t2b}$ 

$$\hat{\boldsymbol{I}}_{t2b}^{m} = \boldsymbol{U}_{t2b} \odot \hat{\boldsymbol{I}}_{t2b}^{s2m} + (1 - \boldsymbol{U}_{t2b}) \odot \hat{\boldsymbol{I}}_{t2b}^{m2e}, \tag{14}$$

where

$$U_{t2b}[i] = \begin{cases} 0, & \text{if } i > m \\ 1, & \text{else} \end{cases}$$
 (15)

Similarly, by vertically flipping the distorted time maps and the time mask, and then according to Eqs. (11), (12) and (14), we can obtain  $\hat{I}_{b2t}^m$ .

# 3.3.2 Self-supervised Losses

We have reconstructed two sets of dual reversed RS images, *i.e.*,  $\hat{I}_{t2b}$ ,  $\hat{I}_{b2t}$  and  $\hat{I}_{t2b}^m$ ,  $\hat{I}_{b2t}^m$ , and thus a loss function  $\ell$  can be imposed

on their corresponding input RS images. The self-supervised loss function is defined as

$$\mathcal{L}_{self} = \mathcal{L}_{se} + \mathcal{L}_{sme},\tag{16}$$

with

$$\mathcal{L}_{se} = \ell(\hat{\mathbf{I}}_{t2b}, \mathbf{I}_{t2b}) + \ell(\hat{\mathbf{I}}_{b2t}, \mathbf{I}_{b2t}),$$

$$\mathcal{L}_{sme} = \ell(\hat{\mathbf{I}}_{t2b}^{m}, \mathbf{I}_{t2b}) + \ell(\hat{\mathbf{I}}_{b2t}^{m}, \mathbf{I}_{b2t}),$$
(17)

where  $\ell$  is the combination of Charbonnier loss [18] and perceptual loss [15] in our experiments, and the hyper-parameters for balancing them are set as 1 and 0.1.

Unlike [32], our improved model  $\mathcal{W}$  directly employs a video frame interpolation method, which does not introduce boundary artifacts as in the bidirectional distortion warping method based on optical flow. Consequently, we no longer require the self-distillation loss in [32], simplifying the two-stage training strategy from [32] into a one-stage training strategy.

# 4 EXPERIMENTS

In this section, our SelfDRSC++ is evaluated on synthetic and real-world RS images, and animated video results can be found from the link *Video Results*. Furthermore, we conducted a more detailed analysis of modules in SelfDRSC++, including the impact of employing different VFI methods within module  $\mathcal{W}$ , as well

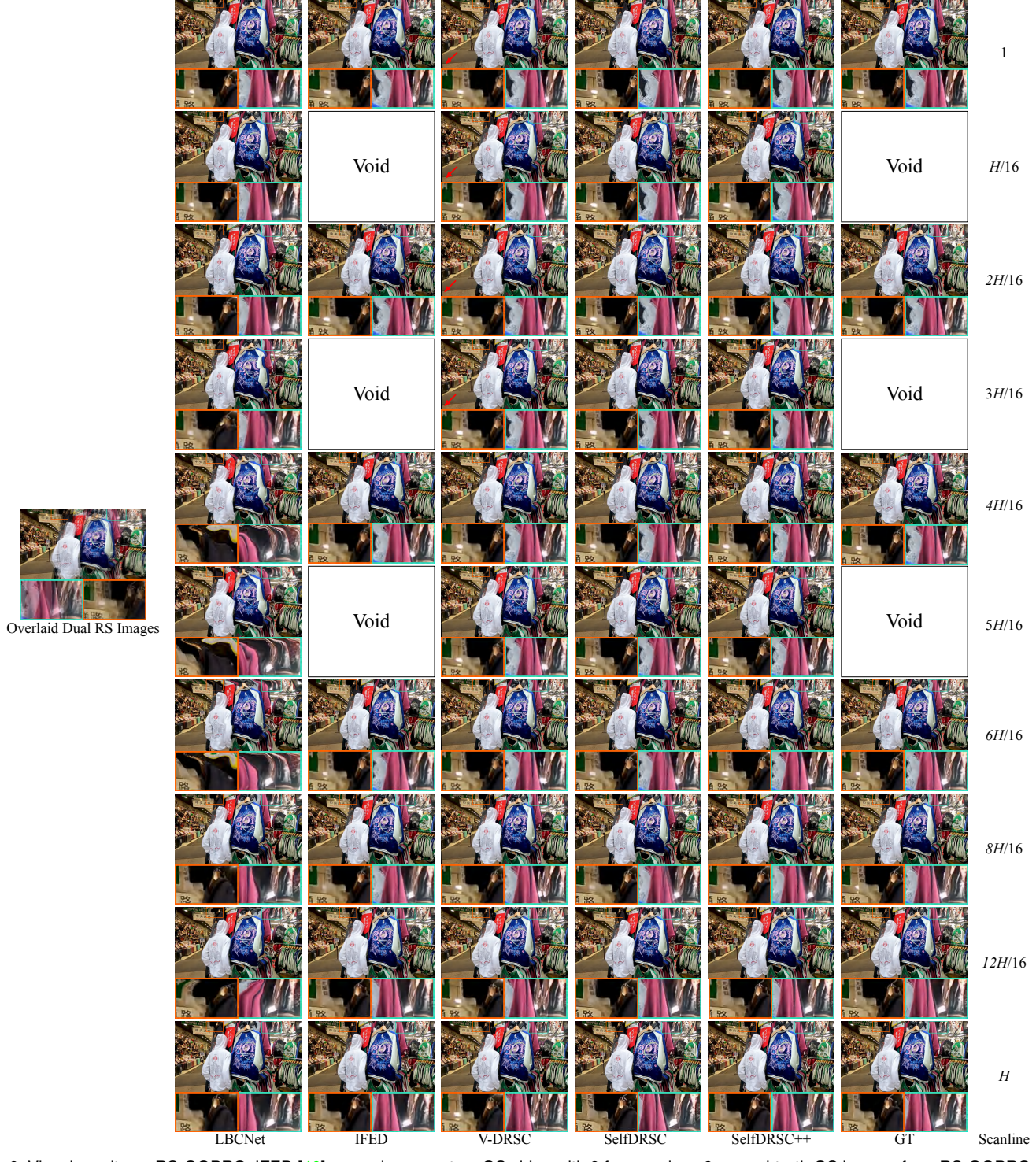


Fig. 6. Visual results on RS-GOPRO. IFED [40] can only generate a GS video with 9 frames since 9 ground-truth GS images from RS-GOPRO are used to train DRSC network in a supervised manner. Our SelfDRSC++ is able to generate GS videos with a higher framerate. In this case, 17 GS frames are generated by SelfDRSC++. Notably, V-DRSC exhibits black boundaries due to the utilization of backward warping, as indicated by the red arrows in the first four rows. It will be better viewed by zooming in.

as the effects of VFI methods training with different variants. Additionally, we performed an ablation analysis on the structure within module  $\mathcal{F}$ .

#### 4.1 Datasets

# 4.1.1 Synthetic Dataset

The synthetic dataset RS-GOPRO from IFED [40] is used for quantitatively evaluating the competing methods. The dataset is

randomly split into 50, 13, and 13 sequences as training, validation, and testing sets, respectively. Furthermore, 9 GS images serve as the ground-truth for both training and testing. This implies that within this dataset, each pair of dual-reversed RS images corresponds to 9 ground-truth GS images. We note that the ground-truth GS images may not be truly collected by a GOPRO camera. As discussed in [32], a VFI method [12] is adopted to generate high framerate GS images, and the interpolated ground-

TABLE 1
Quantitative comparison on the test set of RS-GOPRO [40], where the metrics are computed based on generating 9 GS images for a testing case.

	Method	Inference time (s)	Parameters	PSNR↑ / SSIM↑ / LPIPS↓
Supervised	DUN [23]+RIFE [12]	0.638	14.62M	23.597 / 0.7653 / 0.1670
	RIFE [12]+DUN [23]	4.078	14.62M	20.012 / 0.6520 / 0.1781
	RSSR [8]	0.976	26.03M	22.729 / 0.7283 / 0.1026
	CVR [10]	2.088	42.70M	24.816 / 0.7804 / 0.0738
	IFED [40]	0.177	29.86M	<b>30.681 / 0.9121 /</b> 0.0453
	JAM [11]	0.257	4.73M	24.905 / 0.7891 / 0.0785
	LBCNet [9]	0.233	10.70M	25.193 / 0.7954 / 0.0762
Unsupervised	V-DRSC [30]	0.073	5.26M	25.868 / 0.8338 / 0.0745
	SelfDRSC [32]	0.182	28.75M	28.704 / 0.8886 / 0.0546
	SelfDRSC++	0.156	<b>2.99</b> M	<u>29.584</u> / <u>0.8989</u> / <b>0.0341</b>

TABLE 2

Quantitative comparison on the validation set of RS-GOPRO [40], where the metrics are computed based on 9 GS images for a testing case.

	Method	PSNR↑ / SSIM↑ / LPIPS↓
Supervised	DUN [23]+RIFE [12]	22.313 / 0.7335 / 0.1907
	RIFE [12]+DUN [23]	19.898 / 0.6481 / 0.2073
	RSSR [8]	22.287 / 0.7076 / 0.1052
	CVR [10]	24.286 / 0.7649 / 0.0762
	IFED [40]	<b>30.106 / 0.9046 /</b> <u>0.0460</u>
	JAM [11]	24.294 / 0.7674 / 0.0749
	LBCNet [9]	24.433 / 0.7692 / 0.0741
	V-DRSC [30]	24.470 / 0.7763 / 0.0850
Unsupervised	SelfDRSC [32]	27.818 / 0.8758 / 0.0581
	SelfDRSC++	<u>28.888</u> / <u>0.8898</u> / <b>0.0354</b>

truth GS images may be over-smoothed. Therefore, image quality assessment (IQA) metrics may not be so reliable to assess the performance of competing methods, and we suggest to further referring to visual comparison especially animated videos.

## 4.1.2 Real-world Testing Set

For testing in real-world, Zhong *et al.* [40] built a dual reversed RS image acquisition system in Fig. 1, which consists of a beam-splitter and two RS cameras with dual reversed scanning patterns. Each sample includes two RS distorted images with reversed distortion but without ground-truth.

# 4.2 Implementation Details

Our SelfDRSC++ is trained in an end-to-end manner and only the parameters of  $\mathcal F$  are updated. Within  $\mathcal F$  module, the window size in the matching block is set as 3, which is the same as [21]. The training is done in 150K iterations. The optimization is implemented using AdamW [26] optimizer ( $\beta_1$ =0.9,  $\beta_2$ =0.999) and the initial learning rate is  $2\times 10^{-4}$ , which is gradually reduced to  $5\times 10^{-5}$  with the cosine annealing [25]. Patch size is  $256\times 256$ , and batch size is 16 during the training process. The intermediate time  $t_m$  is randomly sampled between start time  $t_1$  and end time  $t_H$  with sampling interval  $(t_H - t_1)/8$ . During testing, we can specify an arbitrary time instance  $t_m$  for the correction.

#### 4.3 Comparison with State-of-the-art Methods

To keep consistent quantitative evaluation with IFED [40], the output of competing methods should have 9 GS images. Thus, our SelfDRSC++ is compared with methods from three categories. (i) The first category contains cascade methods, where RS correction method DUN [23] for generating one GS image and a VFI model RIFE [12] is adopted for interpolating GS images. Both of them are re-trained on the RS-GOPRO dataset for a fair comparison.

In Tables 1 and 2, both cascade orders are considered, *i.e.*, DUN+RIFE and RIFE+DUN. (ii) The second category contains RS correction methods with multiple output images. There are only two works by adopting the dual reversed RS correction setting, *i.e.*, IFED [40] and Albl *et al.* [1]. Since the source code or experiment results of Albl *et al.* [1] are not publicly available, it is not included in comparison. Besides, we take RSSR [8], CVR [10], JAM [11] and LBCNet [9] into comparison, which are developed for correcting RS distortion from consecutive two RS images with only top-to-bottom scanning. For a fair comparison, they are re-trained based on the RS-GOPRO dataset. (iii) In addition, we also compare with two unsupervised methods, V-DRSC [30] and SelfDRSC [32]. As for quantitative IQA metrics, PSNR, SSIM [36], and LPIPS [39] are employed to evaluate the competing methods.

#### 4.3.1 Results on Synthetic Dataset

Tables 1 and 2 report quantitative comparison, where the IQA metrics are computed based on 9 GS images for each testing case. Our SelfDRSC++, without any ground-truth high framerate GS images during training, achieves better IQA metrics than the other methods except IFED. Although our method exhibits lower PSNR and SSIM compared to IFED, it performs better in terms of LPIPS metric and visual quality in Figs. 5 and 6. As depicted in Fig. 5, the utilization of PSNR and SSIM as evaluation metrics can be misleading, as they may indicate higher values for over-smoothed correction results. In contrast, LPIPS demonstrates a stronger correlation with visual perception. However, considering the presence of interpolated frames introduced by the VFI method in 9 groundtruth GS images as discussed in [32], these IQA metrics may not provide reliable indications of correction performance. Therefore, we recommend relying on visual results, particularly animated videos, to assess correction textures and temporal consistency.

As for the visual quality, reconstructed GS images by competing methods are presented in Fig. 6. IFED [40] can only generate a GS video with 9 frames. Our SelfDRSC++ is able to generate GS videos with a higher framerate. In this case, 17 GS frames are generated by SelfDRSC++ and are better corrected with finer textures. Compared to V-DRSC [30], our results do not exhibit the boundary content loss caused by backward warping operations. In contrast to SelfDRSC [32], our corrected results are more accurate, as can be observed in the green boxes at  $t_m=6H/16$  and 8H/16. In summary, our SelfDRSC++ ensures the correction capability of SelfDRSC while further addressing the inaccuracy of SelfDRSC results near  $t_m=H/2$ . Also, our SelfDRSC++ has fewer network parameters.

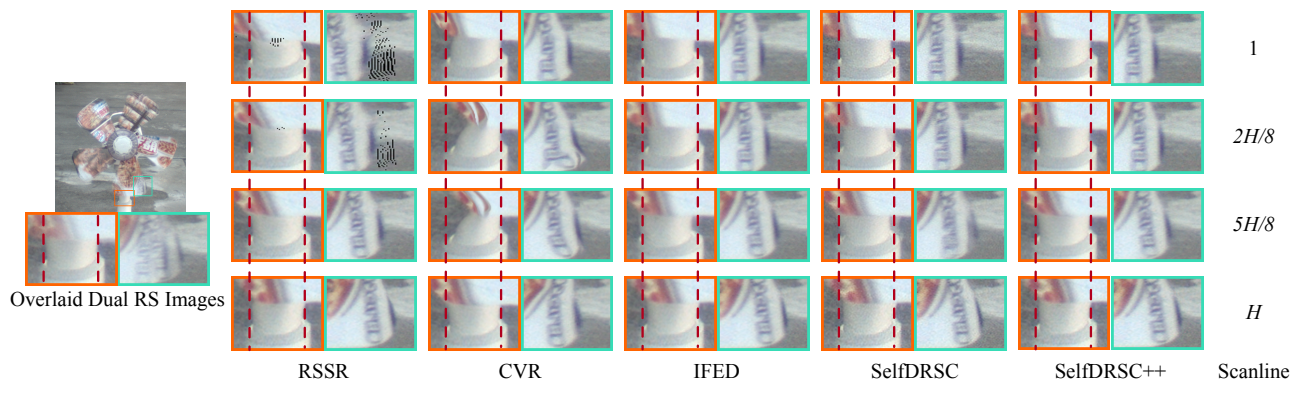


Fig. 7. Comparison of corrected results for moving and stationary objects on real-world RS data. Indicated by red dashed lines, stationary objects corrected by other methods exhibit deformation. As green boxes contain objects in rapid motion, other methods demonstrate abnormal distortion or ghosting effects. In contrast, our SelfDRSC++ outperforms other methods for both stationary and moving objects. Animated videos are available at *Video Results*.

TABLE 3 Ablation results of RS reconstruction module  ${\mathcal W}$  on the test set of RS-GOPRO.

		PSNR↑ / SSIM↑ / LPIPS↓
	[T]	27.761 / 0.8746 / 0.0508
RIFE	[D]	28.870 / 0.8755 / 0.0358
KIFE	[T, R]	26.534 / 0.8456 / 0.0510
	[D, R]	29.584 / 0.8989 / 0.0341
	EMA-VFI	25.296 / 0.8423 / 0.1016
[D D]	IFRNet	25.160 / 0.7554 / 0.0983
[D, R]	AMT	24.308 / 0.7011 / 0.0753
	RIFE	29.584 / 0.8989 / 0.0341

 $\label{eq:table_table} \begin{array}{c} \text{TABLE 4} \\ \text{Ablation study of RS correction module } \mathcal{F} \text{ in SelfDRSC++-}. \end{array}$ 

	PSNR↑ / SSIM↑ / LPIPS↓
w/o matching & updating block	28.455 / 0.8814 / 0.0386
SelfDRSC++ (num=1)	29.233 / 0.8939 / 0.0375
SelfDRSC++ (num=3) (Ours)	29.584 / 0.8989 / 0.0341
SelfDRSC++ (num=5)	29.379 / 0.8972 / 0.0352
SelfDRSC++ (num=7)	29.395 / 0.8966 / 0.0349

TABLE 5
Comparison of different self-supervised strategies.

	PSNR↑ / SSIM↑ / LPIPS↓
SelfDRSC w/o self-distillation	28.411 / 0.8848 / 0.0574
SelfDRSC	28.704 / 0.8886 / 0.0546
SelfDRSC+	28.821 / 0.8902 / 0.0488
SelfDRSC++	29.584 / 0.8989 / 0.0341

# 4.3.2 Results on Real-world Data

In Fig. 7, we provide an example of real-world dual reversed RS images. By examining the overlaid dual RS images, it is evident that the fan pole within the orange box remains stationary, while the fan blades within the green box are rotating at high speed. However, existing correction methods struggle to accurately discern whether objects in the images are distorted. All methods except our SelfDRSC++ have resulted in displacement or distortion, as compared to the orange box in Fig. 7. For objects in rapid motion, such as those in the green box, other methods exhibit abnormal distortion or ghosting at object boundaries. Our SelfDRSC++ ensures that stationary objects are not subject to deformation while effectively correcting the distortion for moving objects. The link *Video Results* provides more video results for further comparisons of visual quality and temporal consistency.





Fig. 8. Visual comparison of RS reconstruction using different RIFE variants with GS frames at times  $t_1$  and  $t_H$ .

 $I_{t2b}$ 

 $I_{b2t}$ 

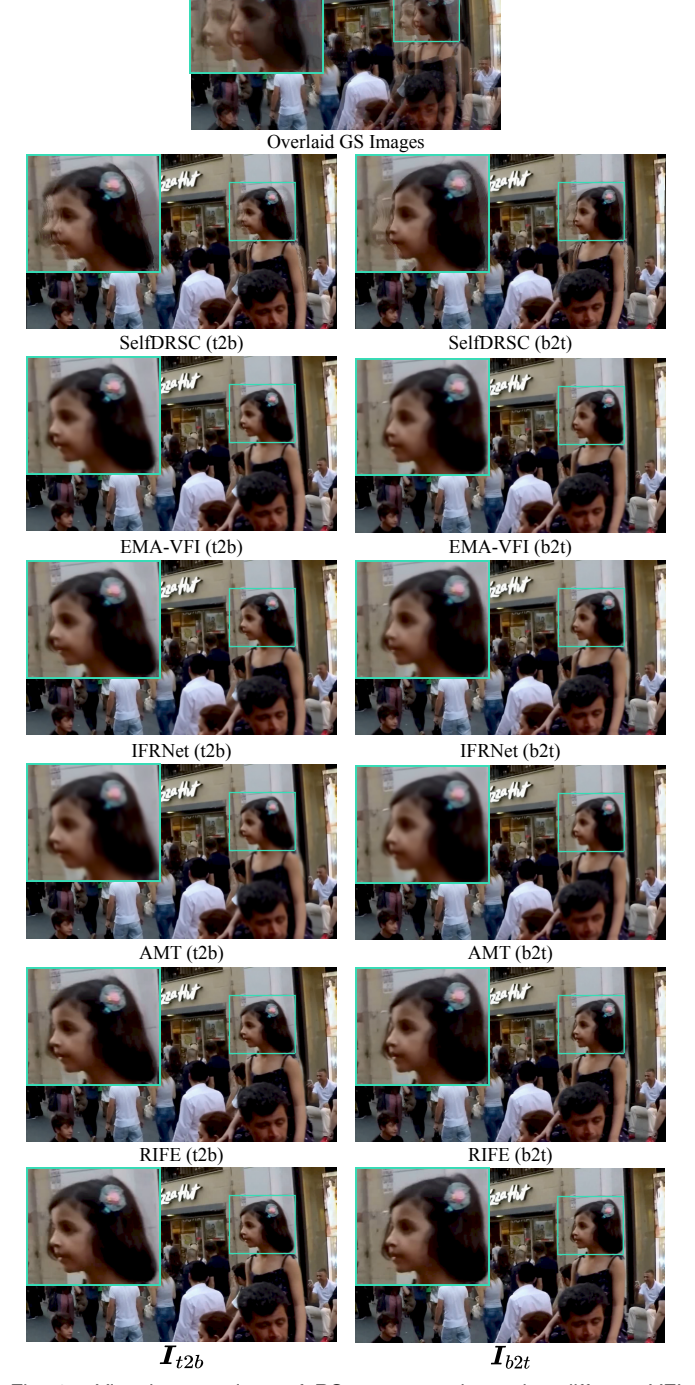


Fig. 9. Visual comparison of RS reconstruction using different VFI methods with GS frames at times  $t_1$  and  $t_H$ .

# 4.4 Ablation Study

For the RS reconstruction module  $\mathcal{W}$ , we demonstrate the effectiveness of different VFI methods and various variants for VFI methods. For the RS correction module  $\mathcal{F}$ , we also examined the effectiveness of the correlation matching module and the number of fields in the GS reconstruction module. We implement the ablation study on these elements. All the IQA metrics are computed based on generating 9 GS images.

For each VFI method W, we can combine the plug-and-play nature of distance indexing and iterative reference-based estimation strategies [41] to form various variants for VFI methods.

Specifically, we denote the variant trained with the time indexing as [T], the variant trained with distance indexing as [D], the variant trained with iterative reference-based estimation as [T, R], and the variant that combines both distance indexing and iterative reference-based estimation as [D, R]. All these trained models are borrowed from [41] without finetuning on the RS dataset, we employ them as W to reconstruct RS for self-supervised learning. We take RIFE [12] as an example. As shown in Table 3, [D, R] RIFE gets the best performance, since it combines both distance indexing and iterative reference-based estimation to solve the ambiguity of speed and direction. In Fig. 8, we present a visual comparison of RS reconstruction results for various variants of RIFE. Our observations reveal that the reconstructions by [D, R] RIFE more closely resemble the original RS images, thus indicating that correction module  $\mathcal{F}$ , trained with [D, R] RIFE (as W), yields the most effective performance.

For different VFI methods in  $\mathcal{W}$ , we use RIFE [12], AMT [21], IFRNet [17] and EMA-VFI [38] as  $\mathcal{W}$ , respectively. Similarly, we use all these methods trained with the combined approach [D, R] as  $\mathcal{W}$ , which are also provided by [41]. From Table 3, [D, R] RIFE achieves the best performance on self-supervised dual reversed rolling shutter correction task. Hence, we use [D, R] RIFE as our RS reconstruction module  $\mathcal{W}$  in the following. Similarly, in Fig. 9, we conduct a visual comparison of RS reconstruction results obtained using different VFI methods. This once again confirms that the better the RS reconstruction by  $\mathcal{W}$ , the more beneficial it is for training  $\mathcal{F}$ .

To validate the role of the correlation matching module within  $\mathcal{F}$  and to evaluate the impact of varying the number of fields, we have created corresponding variants for these factors. These include a variant with the correlation matching module removed, along with the corresponding update block. Additionally, we have set the number of fields as 1, 3, 5, and 7 to study their effects. From Table 4, one can see that setting the number of fields as 3 gets the best performance and we use it as our default setting.

To further substantiate the effectiveness of our novel self-supervised strategy, we integrated the GS reconstruction module W (i.e., RIFE [D, R]) into SelfDRSC [32], dubbing the enhanced model as SelfDRSC+. One can observe from the second row and the sixth row in Fig. 9 that compared to SelfDRSC, our new self-supervised strategy generates more accurate RS reconstructions, which aids the correction module in conducting more effective self-supervised learning. As demonstrated in Table 5, SelfDRSC+ and SelfDRSC++ exhibit superior performance compared to the original SelfDRSC [32]. More importantly, the proposed Self-DRSC++ simplifies the training process, transitioning from a two-stage approach to a single-stage one, eliminating the self-distillation phase while achieving improved performance.

# 5 CONCLUSION

In this paper, we proposed an improved self-supervised learning framework, SelfDRSC++, for correcting dual reversed RS distortion. Our SelfDRSC++ is capable of generating high framerate GS videos by taking dual RS images with dual reverse distortion as input. Compared to the previous version SelfDRSC, SelfDRSC++ has made enhancements on both correction modules  $\mathcal F$  and reconstruction modules  $\mathcal W$ . On the one hand, we have proposed a lightweight correction model  $\mathcal F$  that utilizes a correlation matching block and an updating block, significantly reducing the number of model parameters while improving correction performance. On

the other hand, we have proposed a simpler RS reconstruction module  $\mathcal{W}$ , which is adapted from video frame interpolation method that employs distorted time maps, enabling more accurate RS reconstruction and making the self-supervised learning cycle consistency feasible and effective. Our SelfDRSC++ achieves better results with only one training stage, eliminating the need for self-distillation to mitigate boundary artifacts in the corrected GS images. Extensive experiments have been conducted to validate the effectiveness and generalization capability of our SelfDRSC++ on both synthetic and real-world data.

## REFERENCES

- [1] Cenek Albl, Zuzana Kukelova, Viktor Larsson, Michal Polic, Tomas Pajdla, and Konrad Schindler. From two rolling shutters to one global shutter. In *CVPR*, pages 2505–2513, 2020. 1, 2, 3, 9
- [2] Cenek Albl, Zuzana Kukelova, and Tomas Pajdla. R6p-rolling shutter absolute camera pose. In *CVPR*, pages 2292–2300, 2015.
- [3] Haoran Bai and Jinshan Pan. Self-supervised deep blind video superresolution. *ArXiv preprint arXiv:2201.07422*, 2022. 3
- [4] Wenbo Bao, Wei-Sheng Lai, Chao Ma, Xiaoyun Zhang, Zhiyong Gao, and Ming-Hsuan Yang. Depth-aware video frame interpolation. pages 3703–3712, 2019. 3
- [5] Huaijin Chen, Jinwei Gu, Orazio Gallo, Ming-Yu Liu, Ashok Veeraraghavan, and Jan Kautz. Reblur2deblur: Deblurring videos via self-supervised learning. In *ICCP*, pages 1–9, 2018. 3
- [6] Yen-Kuang Chen, Anthony Vetro, Huifang Sun, and Sun-Yuan Kung. Frame-rate up-conversion using transmitted true motion vectors. In MSPW, pages 622–627, 1998. 3
- [7] Byung-Tae Choi, Sung-Hee Lee, and Sung-Jea Ko. New frame rate upconversion using bi-directional motion estimation. *IEEE TCE*, 46:603– 609, 2000. 3
- [8] Bin Fan and Yuchao Dai. Inverting a rolling shutter camera: Bring rolling shutter images to high framerate global shutter video. In *ICCV*, pages 4228–4237, 2021. 1, 2, 9
- [9] Bin Fan, Yuchao Dai, and Hongdong Li. Learning bilateral cost volume for rolling shutter temporal super-resolution. *IEEE TPAMI*, 2024. 1, 2, 9
- [10] Bin Fan, Yuchao Dai, Zhiyuan Zhang, Qi Liu, and Mingyi He. Context-aware video reconstruction for rolling shutter cameras. In CVPR, pages 17572–17582, 2022. 2, 9
- [11] Bin Fan, Yuxin Mao, Yuchao Dai, Zhexiong Wan, and Qi Liu. Joint appearance and motion learning for efficient rolling shutter correction. In *CVPR*, pages 5671–5681, 2023. 1, 2, 4, 9
- [12] Zhewei Huang, Tianyuan Zhang, Wen Heng, Boxin Shi, and Shuchang Zhou. Real-time intermediate flow estimation for video frame interpolation. In *ECCV*, pages 1–16, 2022. 3, 8, 9, 11
- [13] Bo-Won Jeon, Gun-Ill Lee, Sung-Hee Lee, and Rae-Hong Park. Coarse-to-fine frame interpolation for frame rate up-conversion using pyramid structure. *IEEE TCE*, 49:499–508, 2003. 3
- [14] Huaizu Jiang, Deqing Sun, Varun Jampani, Ming-Hsuan Yang, Erik Learned-Miller, and Jan Kautz. Super Slomo: High quality estimation of multiple intermediate frames for video interpolation. In CVPR, pages 9000–9008, 2018. 3
- [15] Justin Johnson, Alexandre Alahi, and Li Fei-Fei. Perceptual losses for real-time style transfer and super-resolution. In ECCV, pages 694–711, 2016. 3, 7
- [16] Tarun Kalluri, Deepak Pathak, Manmohan Chandraker, and Du Tran. FLAVR: Flow-agnostic video representations for fast frame interpolation. In WACV, pages 2071–2082, 2023. 3
- [17] Lingtong Kong, Boyuan Jiang, Donghao Luo, Wenqing Chu, Xiaoming Huang, Ying Tai, Chengjie Wang, and Jie Yang. IFRNet: Intermediate feature refine network for efficient frame interpolation. In CVPR, pages 1969–1978, 2022. 3, 11
- [18] Wei-Sheng Lai, Jia-Bin Huang, Narendra Ahuja, and Ming-Hsuan Yang. Fast and accurate image super-resolution with deep laplacian pyramid networks. *IEEE TPAMI*, 41(11):2599–2613, 2018. 7
- [19] Yizhen Lao and Omar Ait-Aider. Rolling shutter homography and its applications. *IEEE TPAMI*, 43(8):2780–2793, 2020.
- [20] Hyeongmin Lee, Taeoh Kim, Tae-young Chung, Daehyun Pak, Yuseok Ban, and Sangyoun Lee. AdaCof: Adaptive collaboration of flows for video frame interpolation. pages 5316–5325, 2020. 3
- [21] Zhen Li, Zuo-Liang Zhu, Ling-Hao Han, Qibin Hou, Chun-Le Guo, and Ming-Ming Cheng. AMT: All-pairs multi-field transforms for efficient frame interpolation. In CVPR, pages 9801–9810, 2023. 2, 3, 4, 5, 6, 9,
- [22] Dave Litwiller. CCD vs. CMOS. *Photonics spectra*, 35(1):154–158, 2001.

- [23] Peidong Liu, Zhaopeng Cui, Viktor Larsson, and Marc Pollefeys. Deep shutter unrolling network. In CVPR, pages 5941–5949, 2020. 1, 2, 9
- [24] Peidong Liu, Joel Janai, Marc Pollefeys, Torsten Sattler, and Andreas Geiger. Self-supervised linear motion deblurring. *IEEE Robotics and Automation Letters*, 5(2):2475–2482, 2020. 3
- [25] Ilya Loshchilov and Frank Hutter. SGDR: Stochastic gradient descent with warm restarts. ArXiv preprint arXiv:1608.03983, 2016. 9
- [26] Ilya Loshchilov and Frank Hutter. Decoupled weight decay regularization. ArXiv preprint arXiv:1711.05101, 2017.
- [27] Marci Meingast, Christopher Geyer, and Shankar Sastry. Geometric models of rolling-shutter cameras. ArXiv preprint cs/0503076, 2005.
  1. 2
- [28] Simon Niklaus, Long Mai, and Feng Liu. Video frame interpolation via adaptive separable convolution. pages 261–270, 2017. 3
- [29] Delin Qu, Yizhen Lao, Zhigang Wang, Dong Wang, Bin Zhao, and Xuelong Li. Towards nonlinear-motion-aware and occlusion-robust rolling shutter correction. In *ICCV*, pages 10680–10688, 2023.
- [30] Delin Qu, Bangyan Liao, Huiqing Zhang, Omar Ait-Aider, and Yizhen Lao. Fast rolling shutter correction in the wild. *IEEE TPAMI*, 45(10):11778–11795, 2023. 1, 2, 9
- [31] Dongwei Ren, Kai Zhang, Qilong Wang, Qinghua Hu, and Wangmeng Zuo. Neural blind deconvolution using deep priors. In CVPR, pages 3341–3350, 2020. 3
- [32] Wei Shang, Dongwei Ren, Chaoyu Feng, Xiaotao Wang, Lei Lei, and Wangmeng Zuo. Self-supervised learning to bring dual reversed rolling shutter images alive. In *ICCV*, pages 13086–13094, 2023. 2, 3, 4, 6, 7, 8, 9, 11
- [33] Wei Shang, Dongwei Ren, Yi Yang, Hongzhi Zhang, Kede Ma, and Wangmeng Zuo. Joint video multi-frame interpolation and deblurring under unknown exposure time. In CVPR, pages 13935–13944, 2023. 3
- [34] Zachary Teed and Jia Deng. RAFT: Recurrent all-pairs field transforms for optical flow. In ECCV, pages 402–419, 2020, 1, 2, 3, 4, 5
- for optical flow. In ECCV, pages 402–419, 2020. 1, 2, 3, 4, 5

  [35] Yangguang Wang, Xiang Zhang, Mingyuan Lin, Lei Yu, Boxin Shi, Wen Yang, and Gui-Song Xia. Self-supervised scene dynamic recovery from rolling shutter images and events. arXiv preprint arXiv:2304.06930, 2023. 3
- [36] Zhou Wang, Alan C Bovik, Hamid R Sheikh, and Eero P Simoncelli. Image quality assessment: From error visibility to structural similarity. *IEEE TIP*, 13(4):600–612, 2004.
- [37] Xiangyu Xu, Li Siyao, Wenxiu Sun, Qian Yin, and Ming-Hsuan Yang. Quadratic video interpolation. *NeurIPS*, 32:1–10, 2019.
- [38] Guozhen Zhang, Yuhan Zhu, Haonan Wang, Youxin Chen, Gangshan Wu, and Limin Wang. Extracting motion and appearance via inter-frame attention for efficient video frame interpolation. In CVPR, pages 5682–5692, 2023. 3, 11
- [39] Richard Zhang, Phillip Isola, Alexei A Efros, Eli Shechtman, and Oliver Wang. The unreasonable effectiveness of deep features as a perceptual metric. In CVPR, pages 586–595, 2018.
- [40] Zhihang Zhong, Mingdeng Cao, Xiao Sun, Zhirong Wu, Zhongyi Zhou, Yinqiang Zheng, Stephen Lin, and Imari Sato. Bringing rolling shutter images alive with dual reversed distortion. In ECCV, pages 233–249, 2022. 1, 2, 3, 6, 8, 9
- [41] Zhihang Zhong, Gurunandan Krishnan, Xiao Sun, Yu Qiao, Sizhuo Ma, and Jian Wang. Clearer Frames, Anytime: Resolving velocity ambiguity in video frame interpolation. arXiv preprint arXiv:2311.08007, 2023. 2, 3, 6, 11
- [42] Jun-Yan Zhu, Taesung Park, Phillip Isola, and Alexei A Efros. Unpaired image-to-image translation using cycle-consistent adversarial networks. In *ICCV*, pages 2223–2232, 2017. 3
- [43] Bingbing Zhuang, Quoc-Huy Tran, Pan Ji, Loong-Fah Cheong, and Manmohan Chandraker. Learning structure-and-motion-aware rolling shutter correction. In CVPR, pages 4551–4560, 2019. 1, 2



Wei Shang received the M.E. degree from Tianjin University in 2021. Currently, he is pursuing the Ph.D. degree in computer science and technology at the Harbin Institute of Technology. His research interests are computer vision and deep learning, particularly focusing on rolling shutter correction and video deblurring.



Dongwei Ren received the Ph.D. degree in computer application technology from the Harbin Institute of Technology in 2017 and the Ph.D. degree in computer application technology from The Hong Kong Polytechnic University in 2018. He is currently an associate professor with the School of Computer Science and Technology, Harbin Institute of Technology. His research interests include computer vision and deep learning.



Wangmeng Zuo received the Ph.D. degree in computer application technology from Harbin Institute of Technology, Harbin, China, in 2007. From 2004 to 2006, he was a Research Assistant with the Department of Computing at the Hong Kong Polytechnic University, Hong Kong. From 2009 to 2010, he was a visiting professor with Microsoft Research Asia. He is currently a professor with the School of Computer Science and Technology, Harbin Institute of Technology. He has published over 200 papers in top-tier

academic journals and conferences. His current research interests include image enhancement and restoration, weakly supervised learning, visual tracking, and image classification. He has served as a Tutorial Organizer in ECCV 2016, an Associate Editor of the IET Biometrics, and the Guest Editor of Neurocomputing, Pattern Recognition, the IEEE Transactions on Circuits and Systems for Video Technology, and the IEEE Transactions on Neural Networks and Learning Systems.



Wanying Zhang received the M.E. degree from Tianjin University in 2022. Currently, she is working towards the Ph.D. degree in computer science and technology at the Harbin Institute of Technology. Her research interests are computer vision and deep learning.



Qilong Wang received the Ph.D. degree from the School of Information and Communication Engineering, Dalian University of Technology, China, in 2018. He currently is an associate professor with Tianjin University. His research interests include visual understanding and deep learning, particularly deep models with high-order statistical modeling and self-attention mechanism. He has published more than 40 academic papers in top conferences and referred journal including

ICCV/CVPR/NeurIPS/ECCV and the IEEE Transactions on Pattern Analysis and Machine Intelligence/IEEE Transactions on Image Processing/IEEE Transactions on Circuits and Systems for Video Technology. He is served as an area chair of CVPR 2024.



Pengfei Zhu received the BS and MS degrees from the Harbin Institute of Technology, Harbin, China, in 2009 and 2011, respectively, and the Ph.D. degree from the Hong Kong Polytechnic University, Hong Kong, China, in 2015. He is currently a professor with the College of Intelligence and Computing, Tianjin University. He has published more than 50 academic papers in ICCV, CVPR, ECCV, AAAI, and IJCAI. His research interests are focused on machine learning and computer vision. His research interests are fo-

cused on machine learning and computer vision.